PAPER

Check for updates

Engaging a highly fluorescent conjugated polymer network for probing endogenous hypochlorite in macrophage cells: improved sensitivity *via* signal amplification†

Rikitha S. Fernandes,‡[a] Neelam Gupta,‡[b] Ch Sanjay,[c] Anamika,[b] Ambati Himaja,[c] Balaram Ghosh, [ID] *[c] Biplab Kumar Kuila [ID] *[b] and Nilanjan Dey [ID] *[a]

We have employed a triazine-based conjugated polymer network (CPN) for the selective detection of hypochlorite in a semi-aqueous environment. CPNs have been widely employed in gas capture, separation, and adsorption, but the fluorescent properties of CPNs possessing extensive π-conjugated systems tend to be unexplored. Herein, we report the photophysical properties of the CPN and investigate its sensing capability towards hypochlorite. Spectroscopic investigations reveal that the CPN forms π-stacked aggregates in aqueous medium, while loose aggregates were observed to be formed in hydrophobic solvents. The fluorogenic CPN demonstrates remarkable selectivity *via* fluorescence quenching and a blueshift response towards hypochlorite in a semi-aqueous medium, accompanied by a color change under UV light. Such a turn-off fluorescence response, along with the blue shift upon hypochlorite sensing, was attributed to the oxidation of the sulfur atom of the thiophene functionality of the CPN, consequently resulting in suppression of Intramolecular Charge Transfer (ICT) in the corresponding oxidized adduct. The fluorescence intensity of the CPN exhibits a linear response to hypochlorite concentration, achieving a low detection limit of 1.2 nM. Furthermore, the practical applicability was demonstrated by the detection of hypochlorite in water samples and fluorescent test-paper strips. Additionally, the present system is utilized for bio-imaging of endogenous hypochlorite in RAW 264.7 cells.

Introduction

Hypochlorite (ClO⁻) is widely present in biological environments and industries, playing crucial roles in catalysis. However, its imbalance can trigger diseases such as Alzheimer's, cerebral ischemia, Parkinson's and cancer. Detecting and quantifying ClO⁻ is vital for understanding its cellular impact and disease progression. Numerous fluorescence-based chemosensors for hypochlorite detection have been developed, including metal–organic frameworks (MOFs), polymers, and hybrid materials.[1,2] In parallel, conjugated polymer frameworks (CPFs) or networks (CPNs) or conjugated porous organic polymers (CPOPs) possess unique combinations of properties such as extended π-conjugation, microporosity, and high surface

[a]*Department of Chemistry, Birla Institute of Technology and Science Pilani, Hyderabad Campus, Hyderabad 500078, India. E-mail: nilanjan@hyderabad. bits-pilani.ac.in*

[b]*Department of Chemistry, Institute of Science, Banaras Hindu University, Varanasi, Uttar Pradesh 221005, India. E-mail: bkkuila.chem@bhu.ac.in*

[c]*Epigenetic Research Laboratory, Department of Pharmacy, Birla Institute of Technology and Science Pilani, Hyderabad Campus, Hyderabad 500078, India. E-mail: balaram@hyderabad.bits-pilani.ac.in*
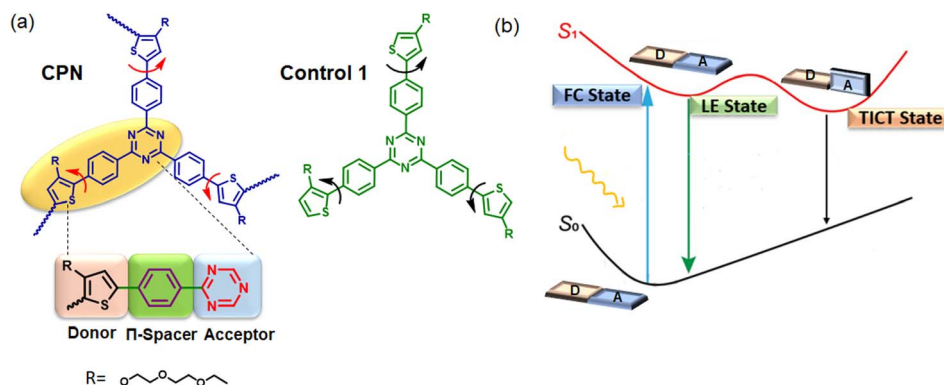
Fig. 1 (a) Schematic representation of the present conjugated polymer network system and the molecular structures of the **CPN** and control 1. (b) Schematic representation indicating the dual emission from TICT–based fluorescent probes.

area, making them promising candidates for various cutting-edge applications.[3] Through careful monomer design, specific binding sites can be introduced, which can significantly boost analyte selectivity.[4] Structurally, they exhibit delocalized electronic structures in their backbones, fostering efficient coupling between optoelectronic segments. These characteristics facilitate highly effective transfer of excitons to lower electron- or energy-acceptor sites along the backbone, leading to either the quenching of fluorescence or the amplification of acceptor signals.[2,5] In direct comparison with their constituent monomer units, CPFs/**CPNs** stand out for their capacity to deliver exceptional signal amplification, owing to their porous and more extended conjugated structures. Additionally, these framework materials often end with low fluorescence quantum yield due to self-quenching *via* aggregation from electron-rich molecular stacks instead of their expected strong fluorescence.[6] One such strategy to improve solubility and fluorescence quantum yield by decreasing π–π stacking is to introduce a long side chain in the backbone of framework materials.

Considering these factors, we have designed a novel triazine-based **CPN** by conjugating a 3-(2-(2-ethoxyethoxy)ethoxy)thiophene (donor) unit with a triazine ring (acceptor) *via* a phenyl ring linker (Fig. 1). The **CPN** was further explored for the detection of hypochlorite in a semi-aqueous environment, and also on paper strips as well as in real life water samples. Furthermore, the probe was used for the detection of hypochlorite in RAW 264.7 cells. Spectroscopic and theoretical investigations provide a thorough elucidation of the sensing mechanism, which involves the oxidation of the thiophene sulfur moiety to sulfone functionality upon interaction with hypochlorite ions. It is noteworthy that our study represents the first report of a triazine-based conjugated polymer network sensor specifically designed for the detection of hypochlorite ions in a semi-aqueous medium.

Experimental section

General

All chemicals (solvents, reagents, and chemicals) were purchased from the best-known local chemical suppliers and used without further purification. FTIR spectra were recorded on a PerkinElmer FT-IR Spectrum BX system and were reported in wave numbers (cm^{-1}). NMR spectra were recorded with a Bruker Avance Neo 400 spectrometer operating at 400 and 100 MHz for ^1H and ^{13}C NMR spectroscopy, respectively. Mass spectra were recorded on a Shimadzu LC-MS. The powder X-ray diffraction (PXRD) pattern was obtained on a Panalytical HighResolution (XRD-I, PW 3040/60) diffractometer using a Cu $K\alpha$ source operated at 45 kV and 30 mA. Gel-permeation chromatography (GPC) was carried out on a Malvern Panalytical (UK) Model-GPC 5140 instrument. The scanning electron microscopy (SEM) image was recorded on an FEI Quanta 400 FEG instrument. Nitrogen adsorption–desorption isotherms were measured at 77 K on a Quantachrome Autosorb-iQ analyzer after the sample was outgassed at 150 °C for 24 h. The UV-Vis spectroscopic studies were carried out on a JASCO (model V-650) UV-Vis spectrophotometer. Fluorescence experiments were performed using a FluoroLog-TM (Horiba Scientific). The fluorescence decay experiment was performed using a time-correlated single photon counting fluorimeter (Horiba Delta flex Modular). The detailed procedure of the sensing studies through spectroscopic methods including sample preparation is given in the ESI.†

Cell culture

Macrophage cells, RAW 264.7 were purchased from the American Type Culture Collection (ATCC, USA). Fetal bovine serum (FBS), trypsin–EDTA, Dulbecco's modified Eagle's medium (DMEM), and penicillin/streptomycin solution were purchased from Himedia Laboratories (Mumbai, India). The DMEM containing fetal bovine serum (10%) and penicillin/streptomycin (100 IU mL^{-1}) was used for sub-culturing RAW 264.7 cells and incubated at 37 °C with 5% CO_2 under a humidified sterile atmosphere. After mounting, the images were captured using a confocal microscope (Leica Microsystems, Germany). The excitation wavelength of the compound was 350 nm, and the emission was observed from 430–480 nm. The Ar laser was used at 20% efficiency and magnified at 40×. The captured images were analyzed using Image J software. Additional studies were carried out following the same protocol (see the ESI†).

Results and discussion

Design and synthesis

Among the conjugated network or framework materials, 1,3,5-triazine-based conjugated CPFs/**CPN**s are emerging as a unique class of functional materials with varieties of applications because of the planar structure of the triazine ring with high nitrogen content and electron deficiency (triazine is a typical acceptor unit) and show novel optical and electrochemical properties.[4,7,8] In this regard, we have synthesized a **CPN**, as illustrated in Scheme 1 (Fig. S1–S4†). The successful synthesis of the **CPN** through polymerization was verified by ^{1}H NMR (Fig. S4†) and GPC (Fig. S5†). Detailed synthesis procedures of each compound and their characterization by ^{1}H NMR study including the polymer are described in the ESI.† Instead of direct D–A bonds, a phenyl ring is employed as an appropriate π-conjugated spacer group in an A–(π–D)$_3$ architecture (Fig. 1). This molecular design was carefully engineered to achieve a wide optical band gap and facilitate effective fluorescence emission in the high-energy spectral region by controlling the formation of local (LE) and charge transfer (CT) excited states. The oxygen atom of the ethylene glycol side chain, which is directly attached to the thiophene ring will further enhance the donor ability of the thiophene moiety through resonance resulting in increased polarizability and better charge transfer. A hybridized local and charge transfer excited state can be produced by combining CT and LE excited state characteristics.[7,9] This should enable strong fluorescence with high quantum efficiency. The side chains in the **CPN**, in principle, may also modify π–π interactions in solution depending on solvent polarity and also in the solid state and enhance fluorescence quantum yield.

Additionally, the presence of thiophene is well-established to amplify both intra- and intermolecular interactions, including van der Waals forces, π–π stacking, hydrogen bonding, and S···S interactions, which result from the greater polarizability due to the presence of sulfur.[10] The oligo(ethylene glycol) side chain will also increase the water dispersibility and biocompatibility of the polymer. In GPC with DMF as eluent, the **CPN** showed $M_n = 26\,103$ and PDI = 2.7 with multimodal distribution in the GPC trace (Fig. S5†). The multimodal distribution and high PDI value may be due to the uncontrolled nature of Pd-catalysed condensation polymerization. In addition, the successful preparation of the **CPN** was verified by the FTIR study (Fig. 2a) which displays strong signals at 1505, 1368, and 811 cm^{-1} corresponding to the triazine ring. This indicates the incorporation of the triazine ring into the polymer by a high degree of polymerization. The emergence of signals at 2855 cm^{-1} and 1109 cm^{-1} attributed to aliphatic C–H and C–O stretching respectively provides additional evidence that the ethylene glycol side chains have been incorporated into the polymer network. X-ray diffraction (XRD) revealed the appearance of a broad hump in the region from 10 to 30° indicating an amorphous structure (Fig. 2b). The **CPN** contains a long side chain attached to the thiophene ring and the introduction of such chains in the polymer backbone may hinder the ordered arrangement of polymer chains leading to the amorphous structure. These side chains will also promote interlayer repulsion and reduce crystallinity. The scanning electron microscope (SEM) image (Fig. 2c) of the prepared bulk sample reveals the nanostructure morphology of interconnected particles. The higher magnification image exhibits the presence of sheet-like structures (Fig. S6†). At 77 K, the porosity of the **CPN** was studied using N$_2$ adsorption–desorption isotherms. The BET surface area of the **CPN** was calculated and the value was 10.76 m^2 g^{-1} (see the ESI†).

The **CPN** shows a sharp rise in N$_2$ uptake at high relative pressures ($P/P_0 > 0.9$) and hysteresis upon desorption indicating the presence of mesopores (Fig. 2d). Such low porosity may be due to the formation of disordered structure where the network structures are non-ideal and probably incomplete with many structural defects. The formation of a disordered structure is also evidenced by the pXRD study conclusively affirming the complete amorphous nature. According to the pore size distribution (PSD), the average pore size for the **CPN** is 3.27 nm. The pore size distribution (PSD) shows a main peak at 3.27 nm with broad peaks in the mesopore region, also suggesting the micro and meso-porosity of the **CPN** (Fig. 2e). In the **CPN**, 3-(2-(2-ethoxyethoxy)ethoxy)thiophene (EET) acts as a donor and triazine as an acceptor (A). Furthermore, we performed DFT calculations (B3LYP functional and 6-31G(d,p) basis set) for the **CPN** (Fig. S7†). The HOMO is mainly delocalized on the EET and benzene ring of one of the molecules with the least contribution from the triazine ring. In contrast, the LUMO is located on the entire two arms of the **CPN** including triazine rings, thereby indicating charge transfer from the HOMO to the LUMO. As a result, it becomes evident that electronic transitions in the **CPN** involve utilizing both local excited (LE) and intramolecular charge transfer (ICT) characteristics.

Nanoaggregate formation in aqueous medium. The probe **CPN** exhibited a sharp fluorescence spectrum in THF with emission maxima at 480 nm whereas, in water, the spectrum appeared to be broad and significantly red-shifted (λ_{max} at 520 nm) along with a reduction in fluorescence intensity (Fig. 3a). To ascertain whether the observed broad spectrum is because of single or multiple photoactive species, we performed excitation spectra measurements at various emission wavelengths in the aqueous medium (Fig. S8†). The excitation spectrum corresponding to the 480 nm emission band displayed a single peak
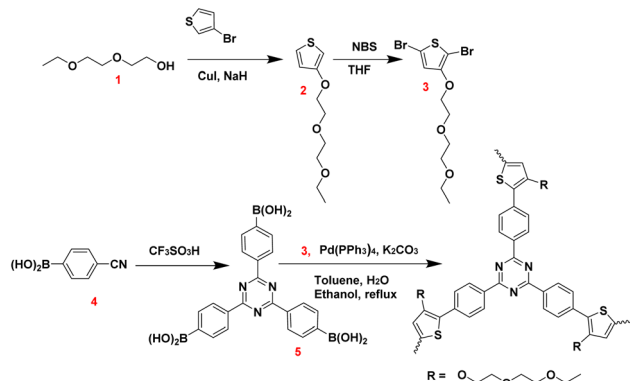
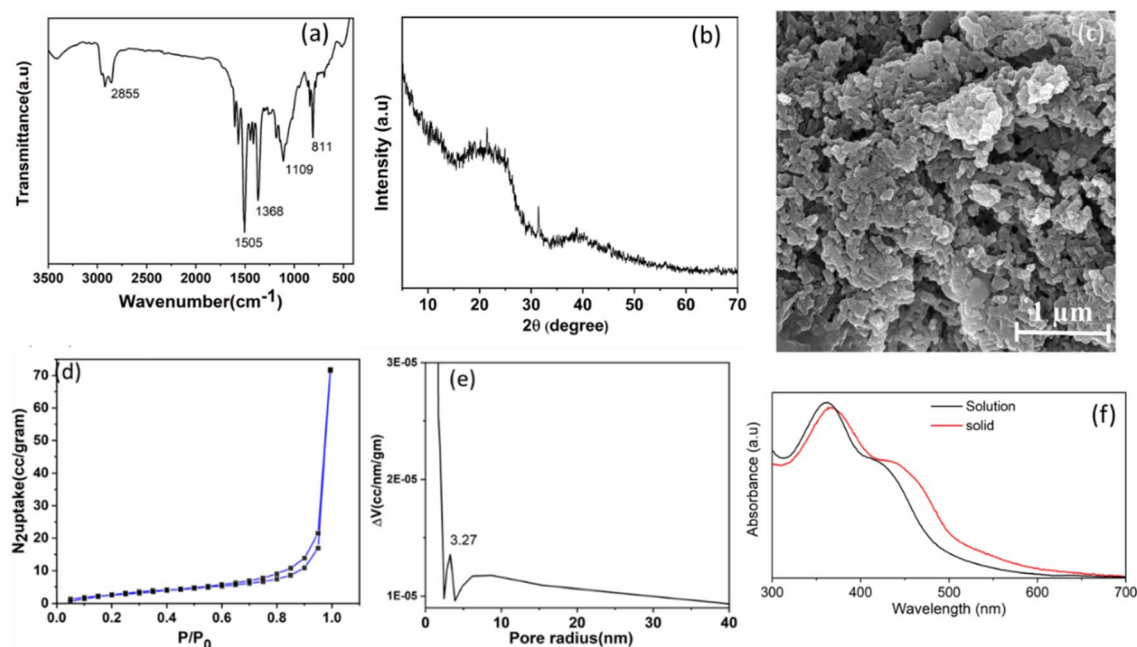**Scheme 1** Synthesis of the **CPN**.

Fig. 2   (a) FTIR spectrum of the **CPN**. (b) Powder XRD pattern of the **CPN**. (c) SEM image of the bulk sample of the **CPN**. (d) Nitrogen adsorption isotherms of the **CPN** measured at 77 K. (e) Pore size distribution from porosity measurement (f) UV-Vis spectra of the **CPN** in solution (THF) and solid state.
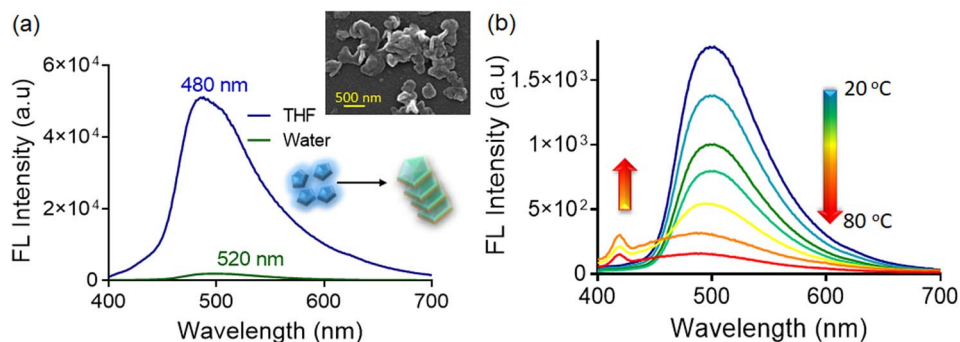

Fig. 3   (a) Fluorescence spectra of the **CPN** (10 μM, λ_{ex} = 365 nm) in THF and water and the FESEM image of the **CPN** in aqueous medium. (b) Temperature-dependent fluorescence spectra of the **CPN** (10 μM, λ_{ex} = 365 nm) in aqueous medium.

at 372 nm whereas, the excitation spectrum for the 520 nm emission exhibited an additional broad peak approximately in the 304–380 nm region. Therefore, we can infer that the emission band at 480 nm is likely associated with monomeric or loosely aggregated species,[11,12] whereas the emission band at approximately 520 nm might be attributed to densely packed aggregates.[13,14] Additionally, we investigated the fluorescence properties of the **CPN** in varying ratios of THF–water mixtures. It was noted that the fluorescence intensity slightly increased in the presence of a 20% water fraction, while a 50% water fraction resulted in fluorescence enhancement of the **CPN**. Further increase in the water fraction, resulted in a significant diminution of fluorescence intensity with a blue shift (~36 nm) from 500 to 464 nm (Fig. S9†). Upon increasing the water fraction to 100%, a bathochromic shift in the emission spectra was observed along with quenched fluorescence. This could

probably be due to the π–π stacked structures of the fluorophores upon aggregation, leading to a reduced band gap with a red shift in their emission maxima.[15,16] Nevertheless, the concentration-dependent fluorescence spectra showed a diminution in the fluorescence intensity at the 520 nm band upon successive dilution (Fig. S10†). Similarly, as the temperature of the solution gradually increased from 20 °C to 80 °C, we noted a remarkable decrease in fluorescence intensity at the 520 nm band, accompanied by a significant blue shift in the emission maxima (Fig. 3b), likely due to the dissociation of pre-existing aggregated structures. We also performed the Dynamic Light Scattering (DLS) experiment of the **CPN** and the hydrodynamic diameter was found to be 223.68 ± 2.25 nm, suggesting the formation of nanoscopic self-agglomerated species (Fig. S11†). The aggregated structures of the **CPN** were also evident in the FE-SEM images (Fig. 3a, inset). The fluorescence decay profile of
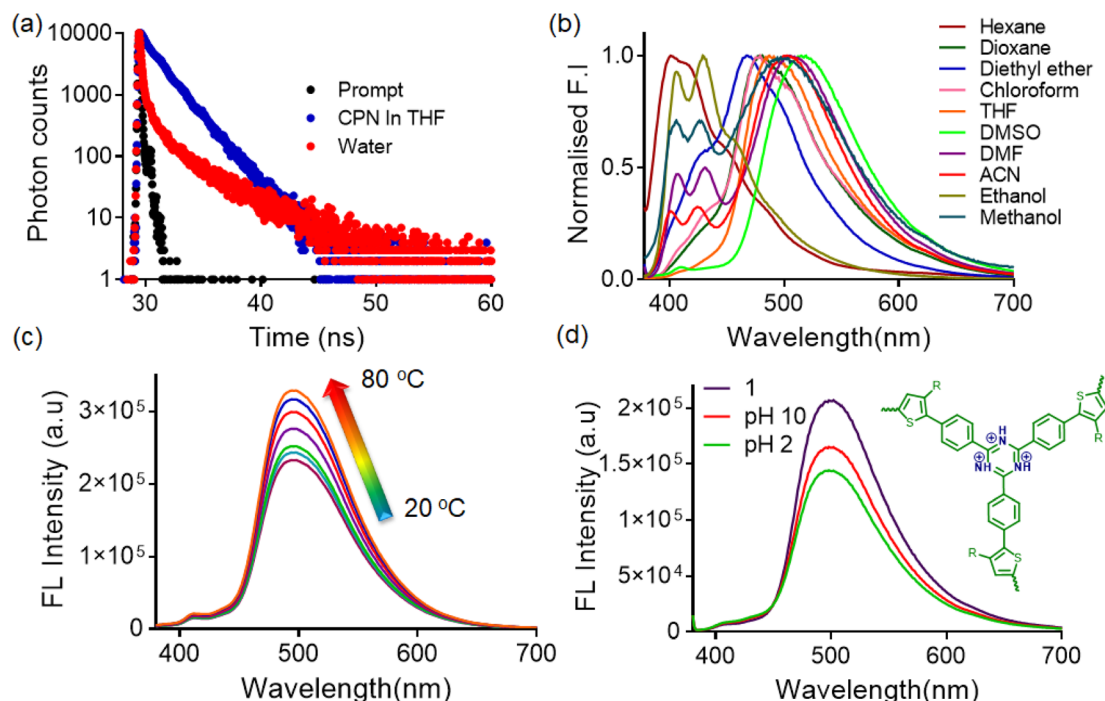
Fig. 4 (a) Fluorescence lifetime decay of the **CPN** (10 μM, λ_{ex} = 365 nm) in THF (at 480 nm) and water (at 520 nm). (b) Normalized fluorescence spectra of the **CPN** (10 μM, λ_{ex} = 365 nm) in different solvents. (c) Temperature-dependent fluorescence spectra of the **CPN** (10 μM, λ_{ex} = 365 nm) in THF : water (1 : 1) medium. (d) Fluorescence spectra of the **CPN** (10 μM, λ_{ex} = 365 nm) in pH 7 (blue line), pH 2 (green line), and pH 10 (red line).

the **CPN** showed a multiexponential decay profile both in THF and water media with an average lifetime of ∼1.48 ns and ∼1.85 ns respectively (Fig. 4a). The presence of photoexcited species with longer average lifetime values is indicative of the self-assembly of probe molecules in the aqueous medium with prominent π–π stacking interactions.[17] Nevertheless, the UV-Vis spectra of the **CPN** in THF (Fig. 2f) exhibit a major absorption band at 362 nm with a hump around 421 nm attributed to π–π* transitions of the conjugated moiety and intramolecular charge transfer (ICT) respectively. Whereas, in the thin film state both the bands show a slight red shift to 368 nm and around 445 nm (Fig. 2f). The ICT may originate from charge transfer interactions between the electron-deficient triazine and the pendant alkoxy group attached to thiophene. Moreover, the **CPN** shows emission colors of blue with high quantum yields (ϕ = 0.4) in THF.

Microenvironment-sensitive fluorescence response. In the THF–water (v/v 1 : 1) mixture, the **CPN** exhibited an emission band at 500 nm, which could probably be due to a long donor–acceptor-type π-conjugated structure.[18] The introduction of the ethylene glycol sidechain in the probe may lead to increased solvation of the excited state (S_1), which consequently results in the excited state of the probe experiencing more significant energy lowering, leading to a reduced energy difference between the ground state (S_0) and the excited state (S_1). This reduction in energy difference contributes to an increase in the emission wavelength (λ_{max}) during fluorescence emission.[7] On the contrary, the monomeric unit of the **CPN** (Control **1**, Scheme S1†) exhibited emission

maxima in the lower wavelength region (∼472 nm) (Fig. S12†), which could probably be due to the lack of extended conjugation as compared to the **CPN**. The substantial differences observed between the **CPN** and the control **1** highlight the enormous potential of employing extended π-conjugated networks for fluorescent applications. In non-polar solvents, such as *n*-hexane, the **CPN** exhibited sharp vibronic bands in the fluorescence spectrum. Upon moving to moderately polar solvents, such as dioxane, a subtle broadening was observed while retaining the presence of two well-defined peaks at 406 and 427 nm (Fig. 4b). In non-polar solvents, the vibronic emission spectra can be attributed to their origin from the planar locally excited (LE) or Frank Condon (FC) states. However, in solvents of comparatively higher polarity, such as CH$_3$CN, DMF, and DMSO, the fluorescence spectra displayed significant broadening and a discernible redshift, probably attributed to the Twisted Intramolecular Charge Transfer (TICT) state.[19,20] Given that the electronic energy levels of the LE and TICT states are not significantly different, these two states coexist in solvents of moderate polarity.[21] Notably, our observations revealed a significant reduction in the fluorescence intensity of the probe in the presence of polar solvents, which could be due to the TICT state being more susceptible to various non-radiative quenching processes than the LE state.[22] To ascertain the involvement of the TICT process, we recorded the temperature-dependent fluorescence response of the compound in THF : water (1 : 1) medium. As the temperature increased, we observed a consistent rise in fluorescence intensity, accompanied by a slight blue shift in emission maxima (Fig. 4c). This observation could plausibly be due to the
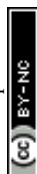
diminishing solvent polarity with increasing temperature, consequently promoting the prevalence of a less twisted molecular conformation of the **CPN**.[23,24] As the temperature increases, higher vibrational bands within the TICT state become thermally accessible, increasing the likelihood of radiative electron transitions from these elevated TICT states back to the ground state.[25] This shift in transition dynamics causes a blue-shift in the emission spectrum, as emissions originating from these higher-energy vibrational bands become more prominent at elevated temperatures.[26] Furthermore, in less polar solvents, the TICT state is destabilized, which results in a larger energy gap between the TICT and Franck–Condon states. This is demonstrated by the observed blue shift in probe emission spectra in the THF : water (1 : 1) medium. We also investigated the effect of pH on the fluorescence response of the **CPN**. In both acidic and basic pH, we observed a significant quenching of fluorescence intensity (Fig. 4d), attributable to changes in the protonation equilibrium of the triazine nitrogens.[27] Notably, the incorporation of the triazine structural unit significantly enhances the electron-accepting capacity in both the excited and protonated states.[28]

Due to the presence of multiple rotatable groups within the **CPN**, we were interested in investigating the effect of viscosity on its photophysical properties. Notably, the fluorescence intensity of the **CPN** exhibits a slight enhancement, along with a slight blue shift with increasing glycerol content (Fig. S13†) in THF : water (1 : 1) medium. Additionally, we also investigated the effect of viscosity in methanol medium (Fig. S14†). We observed a significant fluorescence enhancement at the 426 nm band which is presumably due to the suppression of TICT emission owing to the inhibition of the rotational conformation of the **CPN**, upon increasing the viscosity of the medium.[23]

Response to hypochlorite

Despite significant progress in the development of hypochlorite sensing probes, many existing systems suffer from limitations such as low selectivity, poor sensitivity, high detection limits, and limited applicability in complex biological or environmental matrices (Table S1†). Therefore, in our study, we investigated the sensing behavior of the **CPN** towards hypochlorite. Initially, the fluorescence response of the **CPN** towards hypochlorite in the aqueous medium (buffer pH 7) showed no change upon the addition of NaOCl, probably due to the quenching effect caused by the extensive aggregation of **CPN** molecules in water (Fig. S15†). Since THF : water (v/v 1 : 1) was found to be the optimal solvent mixture in terms of balance between the photophysical response and aggregation of the **CPN**, we investigated the sensing behavior towards hypochlorite in THF : water (1 : 1) medium. When the fluorescence spectra of the **CPN** were recorded with an increasing amount of hypochlorite (0–100 μM), a gradual decrease in emission intensity at the 500 nm band, with a concomitant blue shift (∼15 nm) and an emergence of a new emission band at 424 nm was observed (Fig. 5a). Likewise, fluorescence quenching upon hypochlorite addition was also noted in acetonitrile (Fig. 5b) and ethanol (Fig. S16†) without any blue-shift of the emission maxima. However, the degree of quenching observed was comparatively less pronounced when compared to the quenching observed in the THF : water medium. The saturation in the emission signal
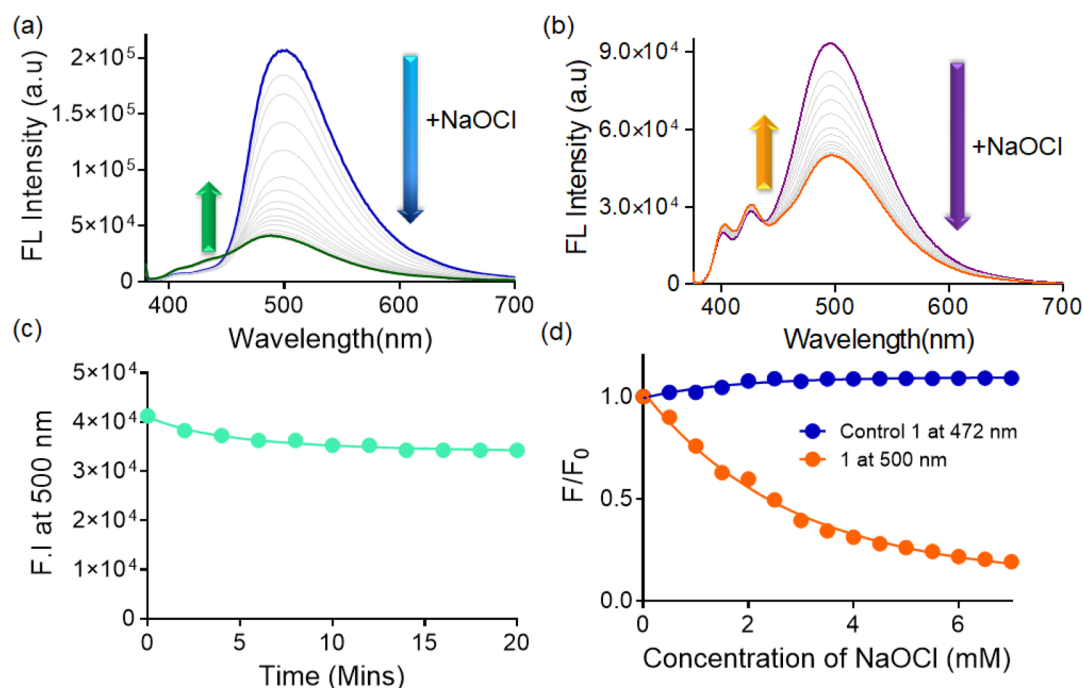
Fig. 5 (a) Fluorescence spectra of the **CPN** (10 μM, λ_{ex} = 365 nm) upon addition of NaOCl (0–100 μM) in THF : water (1 : 1 pH 7) medium. (b) Fluorescence spectra of the **CPN** (10 μM, λ_{ex} = 365 nm) upon addition of NaOCl (0–100 μM) in CH₃CN. (c) Time-dependent changes in fluorescence of the **CPN** (10 μM, λ_{ex} = 365 nm) with NaOCl (100 μM) in THF–water (1 : 1 pH 7) medium. (d) Change in fluorescence intensity of the **CPN** and control 1 (10 μM, λ_{ex} = 365 nm) at 520 nm and 472 nm upon hypochlorite addition (0–100 μM) in THF : water (1 : 1 pH 7) medium.

reached saturation at ~100 μM of hypochlorite addition. The interaction of NaOCl with the **CPN** might result in the formation of a product, which is structurally different from the **CPN** and hence these structural differences could be responsible for the fluorescence quenching observed. A similar observation was evidenced by the Lei group and Honguo *et al.* who correlated the hypochlorite-mediated fluorescence quenching to the formation of sulfone.[29,30] It has also been reported that the fluorescence of aromatic sulfoxides is less due to the non-radiative decay pathways involving the oxidation of sulfur of the thiophene functionality.[31,32] Furthermore, the average lifetime of the **CPN** in THF : water medium decreased negligibly from 1.48 to 1.43 ns upon hypochlorite addition (Fig. S17†). Despite the substantial reduction in emission intensity, there was a negligible decrease in the average lifetime of the **CPN** and it still exhibited a multiexponential decay pattern, upon hypochlorite addition.

Furthermore, the changes in fluorescence intensity at the 500 nm band were plotted against the concentration of added NaOCl. We observed linear regressive plots indicating the reliability of the present system in the quantitative detection of NaOCl and the detection limit was found to be 1.2 nM in the semi-aqueous medium. The time-course analysis was performed by monitoring the changes in fluorescence spectra of the **CPN** upon the addition of 10 equiv. of NaOCl. The kinetic study revealed that the spectral changes reached saturation within 12 minutes of NaOCl addition (Fig. 5c). The long

response time could be possibly due to the co-existence of multiple-step oxidation reactions toward hypochlorite.[33]

To mark the significance of the conjugated polymer network in hypochlorite sensing, we employed control **1**, which lacked the conjugated polymer backbone. There was no significant change in the emission spectra even when a higher amount (0–100 μM) of hypochlorite was added to the solution (Fig. 5d and S18†). This could be due to the absence of Π-conjugated extended functionalities and lack of multiple binding sites and hence lack of signal amplification, consequently resulting in insignificant emission change upon hypochlorite addition. We were further interested in evaluating the effect of temperature on the detection of NaOCl, and hence we recorded temperature-dependent fluorescence spectra of the **CPN** at 20 °C and 80 °C in the presence of hypochlorite (~100 μM). We observed that at lower temperatures, the fluorescence intensity quenches slightly but at higher temperatures, the fluorescence intensity of the probe almost vanishes (Fig. 6a), suggesting that the extent of interaction increases with increasing temperature. This could probably be due to the de-aggregation of pre-formed **CPN** aggregates at higher temperatures, which further improves the sensing behavior towards hypochlorite ions. Additionally, the hydrodynamic diameter significantly decreased to 125.28 ± 4.15 nm, suggesting a disruption of the aggregated structures, upon the addition of NaOCl. To further corroborate this observation, we obtained FESEM images of the probe in the presence of NaOCl. The SEM images confirmed that the larger
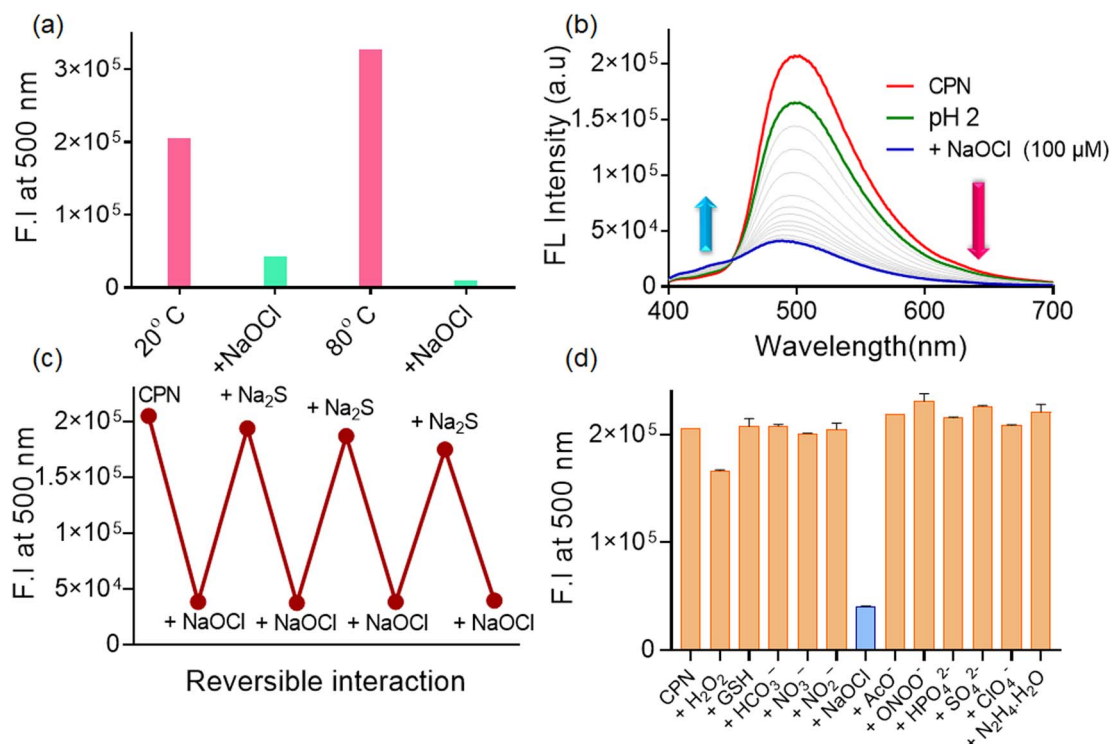
Fig. 6 (a) Temperature-dependent fluorescence spectra of the **CPN** (10 μM, λ_{ex} = 365 nm) at 20 °C and 80 °C in the presence of hypochlorite (~100 μM) in THF−water (1 : 1 pH 7) medium. (b) Fluorescence titration of the **CPN** (10 μM, λ_{ex} = 365 nm) with hypochlorite (0−100 μM) in the presence of pH 2 buffer in THF−water (1 : 1) medium. (c) Reversible interaction of **CPN**. NaOCl with Na₂S in THF−water (1 : 1 pH 7) medium. (d) Change in fluorescence intensity of the **CPN** (10 μM) in the presence of other competing analytes (500 μM) in THF−water (1 : 1 pH 7) medium.

spherical aggregates disintegrated into smaller spherical structures upon NaOCl addition, thereby supporting the dissociation of the preformed nano aggregates (Fig. S19†).

Interestingly, the **CPN** could detect hypochlorite, even in the presence of acidic buffer (pH 2), which was evident by the significant fluorescence quenching (∼5-fold) in the THF : water (1 : 1) medium (Fig. 6b). Furthermore, upon treatment of **CPN**. NaOCl solution with Na₂S, a ∼5-fold fluorescence enhancement was observed, which ultimately retained the original spectral signature of the **CPN**, thereby suggesting a reversible interaction between **CPN**. NaOCl and Na₂S (Fig. 6c). To comment on the specificity, we recorded the fluorescence spectra before and after adding various competitive analytes (10 equiv.) to the semi-aqueous solution of the probe. The tested species didn't show any significant change in the fluorescence response towards the **CPN** (Fig. 6d). These results confirm the selective sensing ability of the **CPN** specifically for hypochlorite without significant interference from other competing analytes.

Mechanistic investigation

The sensing mechanism of the **CPN** towards hypochlorite was comprehensively investigated using FT-IR, ^{1}H NMR, and ESI-MS studies. As depicted in Fig. 7b, a new broad-band appeared at 1404 cm^{-1} in the FT-IR spectra of the probe upon hypochlorite addition, which is the characteristic absorption of the sulfone group, indicating the oxidation of the sulfur in the thiophene unit of the **CPN**.[34] Furthermore, ^{1}H NMR spectra of the **CPN** with and without NaOCl (6 equiv.) were recorded in the DMSO-d_6 medium (Fig. 7c). In the presence of NaOCl, the spectra revealed a noticeable downfield shift of proton signals near the sulfur atom of the thiophene moiety, which could be attributed to the deshielding effect of the O=S=O unit.[34] Furthermore, the ESI-mass spectra also show a prominent peak at m/z = 1046.6 (Fig. 7a), which also provides evidence of the oxidized adduct.

The above results demonstrate that the observed hypochlorite-promoted fluorescence spectral changes were based on the reaction that involved the thiophene functionality of the **CPN**. The initially observed intense fluorescence of the **CPN** can be attributed to the Intramolecular Charge Transfer (ICT) occurring within the π-conjugated system. Upon the introduction of hypochlorite, the oxidation of the thiophene sulfur to sulfone occurs, resulting in the disruption of the donor–acceptor system and native π-conjugation arrangement which induces alterations in the charge distribution within the molecule,[29] thereby inhibiting the ICT process (Fig. 8a).[35] Consequently, this leads to a fluorescence quenching accompanied by the emergence of a blue-shifted emission band, due to the suppression of the ICT transition.[36]
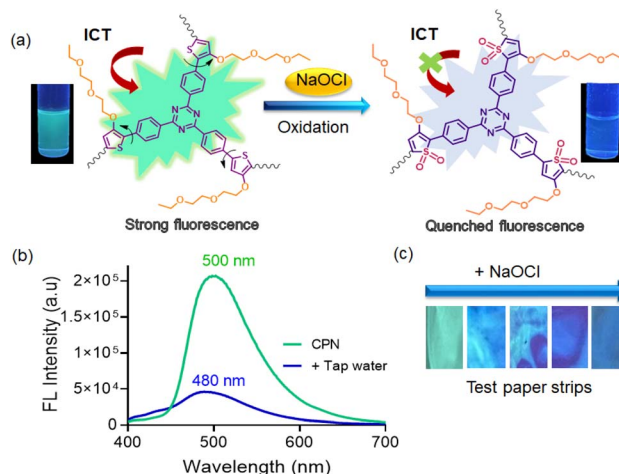
Fig. 8 (a) Plausible sensing mechanism of the **CPN** towards NaOCl. (b) Fluorescence spectra of the **CPN** (10 μM, λ_{ex} = 365 nm) before and after exposure to tap water in THF : water (1 : 1) medium. (c) Images of the color change of pre-coated test paper strips upon exposure to increasing concentrations of hypochlorite (under UV light).
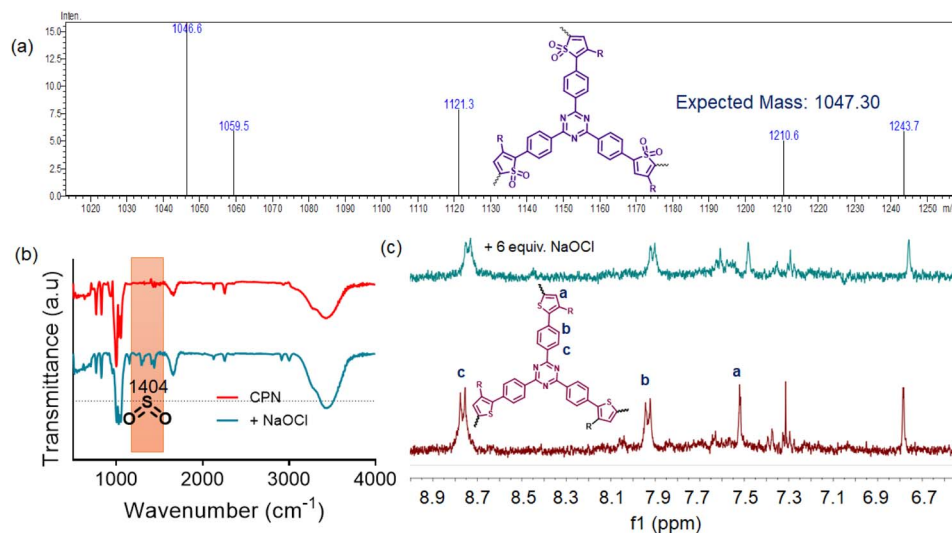
Fig. 7 (a) Mass spectra of probe **CPN**·NaOCl solution. (b) FTIR spectra of the **CPN** with and without the addition of NaOCl (6 equiv.). (c) Partial ^{1}H-NMR of the **CPN** with and without hypochlorite NaOCl (6 equiv.) in DMSO-d_6.

Application to the real-life water samples and test paper strips

Detecting sodium hypochlorite (NaOCl) in water is important due to its pivotal role in ensuring water quality and safety. NaOCl is widely employed as a disinfectant in water treatment processes, making its precise measurement crucial to prevent the proliferation of harmful microorganisms and safeguard public health. In this regard, we conducted hypochlorite detection in real water samples, such as tap water. We performed the fluorescence measurements in the THF–water (tap water, 1 : 1) mixture. In tap water, the probe molecule showed ~3-fold emission quenching as compared to distilled water (Fig. 8b), which could be due to the presence of NaOCl in tap water.

In addition, we prepared a series of NaOCl solutions with known concentrations (10 μM to 100 μM) in tap water. For each concentration, we measured the response of the **CPN** probe sensor under identical conditions. The fluorescence intensity of the probe was plotted against the corresponding NaOCl concentration, resulting in a linear calibration curve over the tested range (Fig. S20†). This curve has a strong correlation coefficient (R^2 = 0.98), and the recovery values were calculated to be in the range of 97.8–102.6%, demonstrating the sensor's high sensitivity to NaOCl concentration in tap water. Furthermore, to validate the practical application of our sensor system in detecting hypochlorite in complex water samples, we applied this standard curve to an industrial waste sample with an unknown NaOCl concentration. The procedure involved collecting the wastewater sample, filtering using a 0.2 μm membrane to remove any particulate matter, and subjecting it to the same experimental conditions as those used for the standard curve generation.[37] Following up, we recorded the fluorescence response of the **CPN** towards the industrial wastewater sample. The fluorescence intensity of the probe was then compared to the standard curve, allowing us to determine the exact concentration of hypochlorite present in the wastewater sample. This approach not only quantifies the hypochlorite levels but also demonstrates the sensor's capability to function effectively in real-life water matrices, where interference from other compounds may be present.

Moreover, due to the limited availability of laboratory facilities in remote areas, there is a critical need to devise alternative methods for detecting hypochlorite that do not rely on sophisticated instrumentation. In this regard, we have employed paper strips coated with the **CPN**. These test strips exhibited bright cyan fluorescence when exposed to UV light (>365 nm). Intriguingly, upon immersion in THF–water (1 : 1) solutions containing increasing concentrations of hypochlorite, the strips showed a remarkable fluorescent color change from cyan to blue (Fig. 8c). Hence, such easily prepared test strips hold promising potential for visually detecting the presence of hypochlorite.

Live cell imaging

Hypochlorite is generated through the peroxidation of chloride ions catalyzed by myeloperoxidase (MPO), mainly located in neutrophils, macrophages, and monocytes.[38] Besides, hypochlorite as reactive oxygen species (ROS) plays crucial roles in physiological and pathological processes.[39] Considering these factors, we explored the potential of the devised probe **CPN** to detect ClO⁻ ions in biological systems (live cells).

Cellular internalization studies. The RAW 264.7 cells were treated with 70 μM **CPN** and the probe got internalized inside the cells after 2 h treatment. Bright blue fluorescence was emitted from the cells at 450 nm and the emission intensity was gradually increased with the increased concentration from 70 μM to 500 μM with an intensity of 43.97 ± 2.3 to 84.54 ± 4.1 respectively (Fig. 9a). Surprisingly, after the incubation period of 4 h, the quenching in the fluorescence was observed with an increase in the concentration of the compound, with an emission intensity of 11.87 ± 1.6 to 0.23 ± 0.05 for concentrations 70 μM to 500 μM respectively as shown in Fig. 9a. The quenching may be due to the reaction time of the **CPN** with the endogenous hypochlorite present in the cells. As per our analysis, a sufficient amount of the **CPN** got internalized after 2 h thereby showing bright blue fluorescence. With the increase in the incubation time of the **CPN**, the **CPN** reacts with the endogenous hypochlorite, thus quenching in fluorescence was observed. The **CPN** concentration of 70 μM was used for further experiments.

Nevertheless, we have evaluated the potential comparison of hypochlorite detection in normal cells to validate the selectivity of our probe. It is well-documented that cancer cells and macrophages typically exhibit elevated levels of reactive oxygen species (ROS), including hypochlorite, due to their altered metabolic and redox states. In our current study, we focused on RAW 264.7 cells (macrophages) to evaluate the probe's ability to detect hypochlorite produced during the immune response. As normal human cells do not produce hypochlorite, we conducted a comparative study using the HEK-293 cell line to test whether the probe would be internalized in non-ROS-producing cells.

From our results (Fig. S21†), we observed that the fluorescence was not detectable in the case of HEK-293 cells when treated with a concentration of 70 μM (of the **CPN**) for 2 h and 4 h, under the same optimized conditions used for our primary experiments. This suggests that the **CPN** probe selectively accumulates in cells that produce more hypochlorites. These findings support the hypothesis that our probe is selective for the cells capable of generating hypochlorite, such as macrophages, and does not interact with normal human cells such as HEK-293 that lack this capability.

Effect of glucose-induced cells/4-ABAH treated cells. The glucose-induced cells treated with the **CPN** (70 μM) had shown complete quenching in fluorescence after a 4 h time point with an emission intensity of 2.79 ± 0.08 (Fig. 9b). Under glucose conditions, the cells produce more hypochlorite endogenously, and the complete quenching in the fluorescence may be due to the reaction of the **CPN** with excess hypochlorite present in the cells. To further validate the sensing application of the **CPN**, the cells were treated with 4-ABAH to eliminate and block the production of hypochlorite inside the cells. As expected, the time-dependent increase in the fluorescence was observed with an emission intensity of 42.39 ± 3.1 and 78.35 ± 4.2 at 2 h and 4 h treatment respectively (Fig. 9c). The unavailability of endogenous hypochlorite in the cells led to the enhancement of emission fluorescence of the internalized **CPN**.
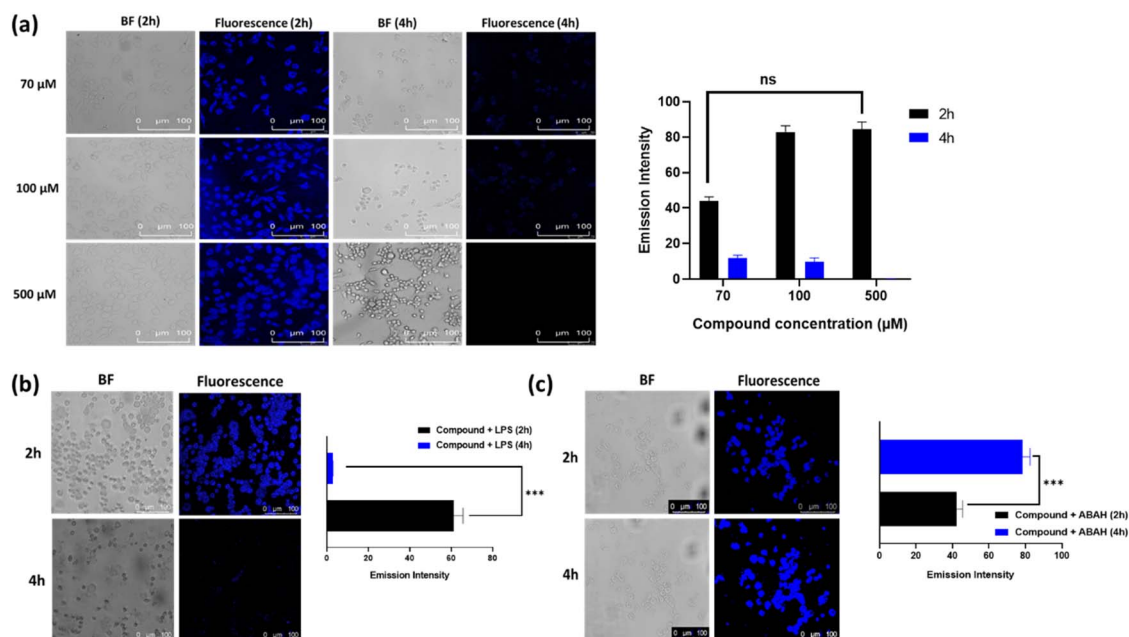
Fig. 9   (a) Confocal fluorescence imaging of endogenous hypochlorite in living RAW 264.7 cells using the **CPN**. Cells were incubated with compounds (70 μM, 100 μM, and 500 μM) for 2 h and 4 h. Blue channel images were obtained from 450 to 480 nm. The average fluorescence emission intensities were quantified from the blue channel images of the cells. (b) Fluorescence images of glucose-exposed cells after 2 h and 4 h treatment with the compound (70 μM), and bar graph displaying the emission intensity. (c) Confocal fluorescence images of RAW 264.7 cells treated with the 4-ABAH blocker (200 μg) followed by **CPN** (70 μM) incubation for 2 h and 4 h with their emission intensities. Scale bar 100 μm. Mean ± SD, $n = 3$. The data are represented as $P < 0.001$ as ***, ns − no significance.

Cytotoxicity by MTT assay and IC50 determination. An MTT assay was conducted to assess the cytotoxicity of the probe in RAW 264.7 cells following the reported procedure.[40] The probe was tested at a concentration of 70 μM across different time points – 2 h, 4 h, 12 h, and 24 h. The results (Fig. S22b†) indicated that the probe exhibited minimal cytotoxicity for a 2 h incubation period for sensing, with cell viability remaining ≥85%. However, at the extended time points of 12 h and 24 h, an increased cytotoxicity was observed (Fig. S22a†). The probe needs to be further modified to reduce its toxicity if the sensing application needs a longer period for the *in vivo* system. Based on these findings, it can be concluded that for sensing applications, using this probe within shorter incubation periods (up to 4 h) should not pose significant toxicity concerns.

Colocalization evaluation using Lyso-Tracker Deep Red

Based on our experimental observations, the **CPN** probe primarily localizes to regions where hypochlorite production is known to occur. In RAW 264.7 macrophages, hypochlorite is predominantly produced in phagolysosomes, which are formed through the fusion of phagosomes and lysosomes during the immune response. Given the role of phagolysosomes in hypochlorite production, we hypothesize that the **CPN** probe accumulates in these compartments, where it can effectively detect hypochlorite as it is generated.

To evaluate the specific accumulation of the probe in phagolysosomes, we conducted a co-localization experiment using Lyso-Tracker Deep Red (0.1 μM), a commercially available
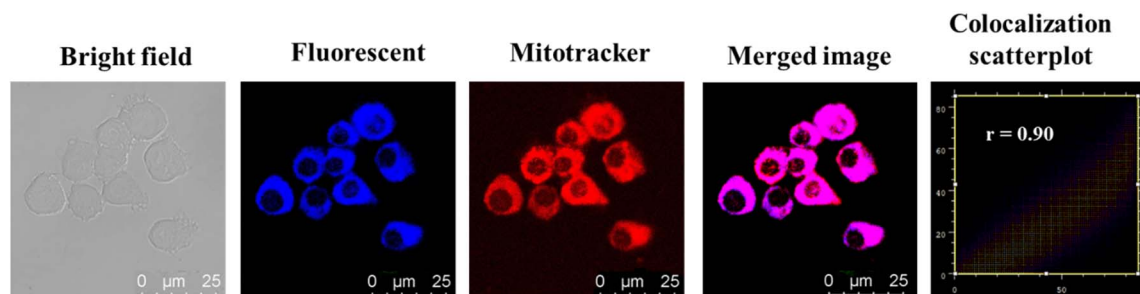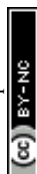

Fig. 10   (a) Bright field and fluorescence images of RAW 264.7 cells treated with the probe **CPN** (70 μM) and Lyso-Tracker Deep Red (0.1 μM). Cells were treated with the **CPN** (70 μM) for 2 h and subsequently with Lyso-Tracker Deep Red (0.1 μM) for 1 h. Scale bar: 25 μm. Images were captured using a Leica DMI8 fluorescence microscope with 40× magnification.

lysosomal tracker, to co-stain RAW 264.7 cells along with the probe (70 μM) (Fig. 10). The fluorescence images of the probe and Lyso-Tracker Deep Red showed significant overlap, with a Pearson's correlation coefficient of 0.90, indicating strong co-localization.

These results demonstrate that the probe localizes well in lysosomes, confirming its accumulation in the appropriate cellular compartment where hypochlorite production occurs.

Conclusion

In the present study, we have introduced a fluorescent conjugated polymer network (CPN), designed specifically for the 'turn off' detection of hypochlorite in a semi-aqueous medium. The CPN was found to form self-assembled aggregated structures in aqueous medium. Moreover, due to the presence of multiple rotatable moieties extending via the polymer backbone, the CPN displayed LE and TICT emissions in non-polar and polar solvents respectively. The response mechanism was elucidated by monitoring changes in its structure using LCMS and ^{1}H NMR spectra, which indicates that the selective interaction of hypochlorite with the CPN was mainly ascribed to the oxidation of thiophene sulfur to sulfone, which consequently results in the disruption of ICT within the CPN. To extend the practicability of the present system, we employed cost-effective test paper strips and also detected hypochlorite in real life water-samples. Furthermore, the bio-imaging experiments demonstrated the sensing capabilities of the CPN in selectively detecting endogenous hypochlorite within RAW 264.7 macrophage cells. To validate the endogenous sensing of hypochlorite in macrophage cells, we have employed glucose-induced cells so that the endogenous hypochlorite production increases. On the other hand, we have also used 4-ABAH as a hypochlorite inhibitor. In both cases, we found that the CPN could selectively detect hypochlorite ions endogenously.

Data availability

The authors confirm that the data will be available on request.

Conflicts of interest

The authors declare no conflict of interest.

Acknowledgements

References

1 Z. Meng and K. A. Mirica, Covalent Organic Frameworks as Multifunctional Materials for Chemical Detection, *Chem. Soc. Rev.*, 2021, **50**(24), 13498–13558.

2 D. T. McQuade, A. E. Pullen and T. M. Swager, Conjugated Polymer-Based Chemical Sensors, *Chem. Rev.*, 2000, **100**(7), 2537–2574.

3 A. Giri, Y. Khakre, G. Shreeraj, T. K. Dutta, S. Kundu and A. Patra, The Order–Disorder Conundrum: A Trade-off between Crystalline and Amorphous Porous Organic Polymers for Task-Specific Applications, *J. Mater. Chem. A*, 2022, **10**(33), 17077–17121.

4 K. M. Omer, S.-Y. Ku, Y.-C. Chen, K.-T. Wong and A. J. Bard, Electrochemical Behavior and Electrogenerated Chemiluminescence of Star-Shaped D–A Compounds with a 1,3,5-Triazine Core and Substituted Fluorene Arms, *J. Am. Chem. Soc.*, 2010, **132**(31), 10944–10952.

5 B. Liu and G. C. Bazan, Homogeneous Fluorescence-Based DNA Detection with Water-Soluble Conjugated Polymers, *Chem. Mater.*, 2004, **16**(23), 4467–4476.

6 R. S. Fernandes and N. Dey, Polarity-Independent Temperature-Induced Reversible Fluorescence Switching of Organic Nanoparticles: Application to Intracellular Temperature Imaging, *ACS Appl. Nano Mater.*, 2023, **6**(7), 5168–5176.

7 N. Gupta, M. R. Nagar, Anamika, P. Gautam, B. Maiti, J.-H. Jou and B. K. Kuila, Triazine and Thiophene-Containing Conjugated Polymer Network Emitter-Based Solution-Processable Stable Blue Organic Leds, *ACS Appl. Polym. Mater.*, 2022, **5**(1), 130–140.

8 S. Bandyopadhyay, N. Gupta, A. Joshi, A. Gupta, R. K. Srivastava, B. K. Kuila and B. Nandan, Solid Polymer Electrolyte Based on an Ionically Conducting Unique Organic Polymer Framework for All-Solid-State Lithium Batteries, *ACS Appl. Energy Mater.*, 2023, **6**(8), 4390–4403.

9 H. Usta, D. Alimli, R. Ozdemir, S. Dabak, Y. Zorlu, F. Alkan, E. Tekin and A. Can, Highly Efficient Deep-Blue Electroluminescence Based on a Solution-Processable A–π–D–π–A Oligo(p-Phenyleneethynylene) Small Molecule, *ACS Appl. Mater. Interfaces*, 2019, **11**(47), 44474–44486.

10 T. Kusukawa and M. Fujita, Self-Assembled m6L4-Type Coordination Nanocage with 2,2′-Bipyridine Ancillary Ligands. Facile Crystallization and X-Ray Analysis of Shape-Selective Enclathration of Neutral Guests in the Cage, *J. Am. Chem. Soc.*, 2002, **124**(45), 13576–13582.

11 H. V. Barkale and N. Dey, Phenazine-Based Fluorescence Probes for Simultaneous Sensing of Silver and Iodide Ions, *J. Mol. Struct.*, 2023, 137427.

12 S. Paul, S. Mondal and N. Dey, Improved Analytical Performance of an Amphiphilic Probe upon Protein Encapsulation: Spectroscopic Investigation along with Computational Rationalization, *ACS Appl. Bio Mater.*, 2023, **6**(4), 1495–1503.

13 R. S. Fernandes and N. Dey, Oxidized Bis(Indolyl)Methane Derivatives with Diverse Signaling Units: An Excitation-

Dependent Fluorescence Response toward Heavy Metal Pollutants in an Aqueous Medium, *Ind. Eng. Chem. Res.*, 2023, **62**(50), 21536–21545.

14 R. S. Fernandes and N. Dey, Metal Ion Responsive Bifunctional Bis(Indolyl)Methane Derivative: Excitation-Triggered Alteration in the Sensing Behavior, *Mater. Chem. Phys.*, 2023, **302**, 127637.

15 S. Mukherjee and P. Thilagar, Fine-tuning Dual Emission and Aggregation-induced Emission Switching in NPI–BODIPY DYADS, *Chem.–Eur. J.*, 2014, **20**(29), 9052–9062.

16 F. Song, Z. Xu, Q. Zhang, Z. Zhao, H. Zhang, W. Zhao, Z. Qiu, C. Qi, H. Zhang, H. H. Sung, I. D. Williams, J. W. Lam, Z. Zhao, A. Qin, D. Ma and B. Z. Tang, Highly Efficient Circularly Polarized Electroluminescence from Aggregation-induced Emission Luminogens with Amplified Chirality and Delayed Fluorescence, *Adv. Funct. Mater.*, 2018, **28**(17), 1800051.

17 R. S. Fernandes, J. Kumari, D. Sriram and N. Dey, Fluorescent Nanoassembly of Tetrazole-Based Dyes with Amphoteric Surfactants: Investigation of Cyanide Sensing and Antitubercular Activity, *ACS Appl. Bio Mater.*, 2023, **6**(10), 4158–4167.

18 Y. Fu, W. Yu, W. Zhang, Q. Huang, J. Yan, C. Pan and G. Yu, Sulfur-Rich Covalent Triazine Polymer Nanospheres for Environmental Mercury Removal and Detection, *Polym. Chem.*, 2018, **9**(30), 4125–4131.

19 R. S. Fernandes and N. Dey, A Combinatorial Effect of TICT and Aie on Bisulfate Detection Using a Pyrenylated Charge-Transfer Luminogen, *Mater. Res. Bull.*, 2023, **163**, 112192.

20 B. Chettri, S. Jha and N. Dey, Unique CT Emission from Aryl Terpyridine Nanoparticles in Aqueous Medium: A Combined Effect of Excited State Hydrogen Bonding and Conformational Planarization, *J. Photochem. Photobiol.*, 2023, **435**, 114210.

21 J. Yang, Q. He, H. Lin, J. Fan and F. Bai, Characteristics of Twisted Intramolecular Charge-Transfer State in a Hyperbranched Conjugated Polymer, *Macromol. Rapid Commun.*, 2001, **22**(14), 1152.

22 P. Das, A. Kumar, A. Chowdhury and P. S. Mukherjee, Aggregation-Induced Emission and White Luminescence from a Combination of π-Conjugated Donor–Acceptor Organic Luminogens, *ACS Omega*, 2018, **3**(10), 13757–13771.

23 G. S. Kottas, L. I. Clarke, D. Horinek and J. Michl, Artificial Molecular Rotors, *Chem. Rev.*, 2005, **105**(4), 1281–1376.

24 V. A. Fonseca Deichmann, V. Yakutkin, S. Baluschev and L. Akcelrud, Optical Tuning of the Fluorescence Spectrum of a π-Conjugated Polymer through Excitation Power, *J. Phys. Chem. B*, 2011, **115**(20), 6385–6394.

25 C. Cao, X. Liu, Q. Qiao, M. Zhao, W. Yin, D. Mao, H. Zhang and Z. Xu, A Twisted-Intramolecular-Charge-Transfer (TICT) Based Ratiometric Fluorescent Thermometer with a Mega-Stokes Shift and a Positive Temperature Coefficient, *Chem. Commun.*, 2014, **50**(99), 15811–15814.

26 Z. R. Grabowski, K. Rotkiewicz and W. Rettig, Structural Changes Accompanying Intramolecular Electron Transfer: Focus on Twisted Intramolecular Charge-Transfer States and Structures, *Chem. Rev.*, 2003, **103**(10), 3899–4032.

27 W. Zhang, F. Xin, Y. Chen and X. Wang, A Fast Acid-Responsive Fluorescent Porous Polymer for Acid-Modified Gas Detection and Optical Anti-Counterfeiting, *Eur. Polym. J.*, 2023, **193**, 112102.

28 F. Elbe, J. Keck, A. P. Fluegge, H. E. Kramer, P. Fischer, P. Hayoz, D. Leppard, G. Rytz, W. Kaim and M. Ketterle, Photochemical and Photophysical Deactivation of 2,4,6-Triaryl-1,3,5-Triazines, *J. Phys. Chem. A*, 2000, **104**(35), 8296–8306.

29 H. Guo, J. Lin, L. Zheng and F. Yang, An Effective Fluorescent Sensor for CLO⁻ in Aqueous Media Based on Thiophene-Cyanostilbene Schiff-Base, *Spectrochim. Acta, Part A*, 2021, **256**, 119744.

30 L. Wang, X. Chen, Q. Xia, R. Liu and J. Qu, Deep-Red Aie-Active Fluorophore for Hypochlorite Detection and Bioimaging in Live Cells, *Ind. Eng. Chem. Res.*, 2018, **57**(23), 7735–7741.

31 S. Malashikhin and N. S. Finney, Fluorescent Signaling Based on Sulfoxide Profluorophores: Application to the Visual Detection of the Explosive TATP, *J. Am. Chem. Soc.*, 2008, **130**(39), 12846–12847.

32 E. L. Dane, S. B. King and T. M. Swager, Conjugated Polymers That Respond to Oxidation with Increased Emission, *J. Am. Chem. Soc.*, 2010, **132**(22), 7758–7768.

33 S. Wang, B. Zhang, W. Wang, G. Feng, D. Yuan and X. Zhang, Elucidating the Structure–Reactivity Correlations of Phenothiazine-based Fluorescent Probes toward CLO⁻, *Chem.–Eur. J.*, 2018, **24**(32), 8157–8166.

34 Z. Zhao, X. Chen, Q. Wang, T. Yang, Y. Zhang and W. Z. Yuan, Sulfur-Containing Nonaromatic Polymers: Clustering-Triggered Emission and Luminescence Regulation by Oxidation, *Polym. Chem.*, 2019, **10**(26), 3639–3646.

35 M. Vedamalai, D. Kedaria, R. Vasita and I. Gupta, Oxidation of Phenothiazine Based Fluorescent Probe for Hypochlorite and Its Application to Live Cell Imaging, *Sens. Actuators, B*, 2018, **263**, 137–142.

36 Y.-S. Lee, J. J. Lee, D. Gil, J. Kang, K.-T. Kim and C. Kim, Fast-Responsive and Multi-Applicable Fluorescent Turn-off Chemodosimeter for Monitoring Hypochlorite: Application to Test Strips, Water Samples, Disinfectants and Bioimaging, *J. Ind. Eng. Chem.*, 2023, **125**, 71–79.

37 A. Piasecka, R. Bernstein, F. Ollevier, F. Meersman, C. Souffreau, R. M. Bilad, K. Cottenie, L. Vanysacker, C. Denis and I. Vankelecom, Study of Biofilms on PVDF Membranes after Chemical Cleaning by Sodium Hypochlorite, *Sep. Purif. Technol.*, 2015, **141**, 314–321.

38 P. A. Kim, D. Choe, H. So, S. Park, B. Suh, S. Jeong, K.-T. Kim, C. Kim and R. G. Harrison, *Spectrochim. Acta, Part A*, 2021, **261**, 120059.

39 Y. Chen, T. Wei, Z. Zhang, W. Zhang, J. Lv, T. Chen, B. Chi, F. Wang and X. Chen, A Mitochondria-Targeted Fluorescent Probe for Ratiometric Detection of Hypochlorite in Living Cells, *Chin. Chem. Lett.*, 2017, **28**(10), 1957–1960.

40 S. Pulya, A. Himaja, M. Paul, N. Adhikari, S. Banerjee, G. Routholla, S. Biswas, T. Jha and B. Ghosh, Selective HDAC3 Inhibitors with Potent In Vivo Antitumor Efficacy against Triple-Negative Breast Cancer, *J. Med. Chem.*, 2023, **66**(17), 12033–12058.